

THE STAR FORMATION HISTORY OF THE LARGE MAGELLANIC CLOUD

JASON HARRIS

National Optical Astronomy Observatory, 950 North Cherry Ave., Tucson, AZ, 85719

AND

DENNIS ZARITSKY

Steward Observatory, 933 North Cherry Ave., Tucson, AZ, 85721

Accepted for Publication in AJ

ABSTRACT

We present the first-ever global, spatially-resolved reconstruction of the star formation history (SFH) of the Large Magellanic Cloud (LMC), based on the application of our StarFISH analysis software to the multiband photometry of twenty million of its stars from the Magellanic Clouds Photometric Survey. The general outlines of our results are consistent with previously published results: following an initial burst of star formation, there was a quiescent epoch from approximately 12 to 5 Gyr ago. Star formation then resumed and has proceeded until the current time at an average rate of roughly $0.2 M_{\odot} \text{ yr}^{-1}$, with temporal variations at the factor-of-two level. The re-ignition of star formation about 5 Gyr ago, in both the LMC and SMC, is suggestive of a dramatic event at that time in the Magellanic system. Among the global variations in the recent star formation rate are peaks at roughly 2 Gyr, 500 Myr, 100 Myr and 12 Myr. The peaks at 500 Myr and 2 Gyr are nearly coincident with similar peaks in the SFH of the Small Magellanic Cloud, suggesting a joint history for these galaxies extending back at least several Gyr. The chemical enrichment history recovered from our StarFISH analysis is in broad agreement with that inferred from the LMC's star cluster population, although our constraints on the ancient chemical enrichment history are weak. We conclude from the concordance between the star formation and chemical enrichment histories of the field and cluster populations that the field and cluster star formation modes are tightly coupled.

Subject headings: galaxies: evolution — galaxies: stellar content — galaxies: Magellanic Clouds — galaxies: individual: Large Magellanic Cloud

1. INTRODUCTION

The LMC is an important target in the effort to understand the stellar populations of galaxies, due to its close proximity, favorable viewing angle, and ongoing star-formation activity. Detailed examination of the LMC's stellar content began in the 1960s with much of it focused on the star cluster population. Hodge (1960, 1961) surveyed populous clusters in the LMC, finding that while 35 of the clusters are similar in age to the population of globular clusters in the Milky Way, the LMC contains 23 populous clusters that are clearly much younger than any Milky Way globular cluster. This observation suggested that the star formation history (SFH) of the LMC might be fundamentally different than that of the Milky Way. Age-dating of LMC clusters via isochrone fitting to color-magnitude diagrams (CMDs) commenced with the dawn of the CCD era, and by 1989 over 100 LMC clusters had been so analyzed (Sagar & Pandey 1989). The age-metallicity relation (AMR) of the LMC's star clusters contains some perplexing features, such as the lack of clusters between 5 and 12 Gyr old (Da Costa 1991; Olszewski et al. 1996; Piatti et al. 2002), and a wide metallicity dispersion among the young ($t < 3$ Gyr) clusters (*e.g.*, Geisler et al. 2003). These features provide clues to the history of star formation in the LMC, but their interpretation has proved difficult.

As useful as star clusters are, a complete understanding of the LMC's star formation history (SFH) requires analysis of its entire stellar population. Early work on the LMC's field population included the analysis of the

spatial distribution of Cepheid variables in the LMC, grouped by age (Payne-Gaposhkin 1972). She found abundant evidence for a complex, spatially-variable SFH, albeit over a relatively limited age interval of 10^7 – 10^8 yr. The Cepheid analysis was updated by the MACHO project (Alcock et al. 1999), who found a burst of star formation 115 Myr ago.

Understanding star formation in the LMC across its entire history requires disentangling the complex admixture of its field stellar populations, a task that was long regarded as nearly impossible (*e.g.*, Schwarzschild 1958, p. 2). However, by the 1980s, our understanding of stellar evolution and the stellar initial mass function (IMF) coupled with the improvements in computing and detector technology made such an analysis possible. The key to disentangling the complex mix of stellar populations in the LMC lies in the quantitative comparison of observed CMDs to synthetic CMDs built by populating theoretical isochrones according to an adopted IMF and an input model star formation history. Some of the earliest synthetic-CMD efforts employed the “R method”, which is a statistical comparison of observed and synthetic CMDs using the main sequence luminosity function and ratios of star counts in age-sensitive regions of the CMD, such as the red giant branch and the subgiant region (Bertelli et al. 1992).

All modern synthetic CMD methods are essentially generalizations of the R method: instead of a one-dimensional luminosity function and star-count ratios in a few select regions of the CMD, the full N-dimensional distribution of stars in one or more CMDs is employed in

the analysis. Much of the recent work on reconstructing the SFH of the LMC has utilized data from the Hubble Space Telescope (HST), which provides CMDs that reach well below the ancient main sequence turn-off (MSTO; Gallagher et al. 1996; Geha et al. 1998; Holtzman et al. 1999; Olsen 1999; Smecker-Hane et al. 2002), even in the crowded bar regions. Such depth is difficult to achieve with ground-based observations due to the limited resolution, especially in the crowded regions of the LMC bar. Reaching below the ancient MSTO is important not only for constraining the ancient SFH, but also for measuring the low-mass stellar IMF, which provides the critical conversion factor for ground-based stellar photometry between the number of bright stars observed and the total stellar mass present.

Among the HST studies targeting the bar, there is a remarkable consensus regarding the general outlines of the LMC’s early SFH. The “Age Gap” seen among the LMC’s star clusters is also evident in the field populations of the bar: following an initial burst of star formation, the LMC experienced a long quiescent epoch that lasted several Gyr. Then, 4 or 5 Gyr ago, star formation resumed and continues to this day. The question of the Age Gap among field populations in the LMC disk is more ambiguous. The study of some areas of the disk seem to demand a quiescent epoch (cf. Dolphin 2000), while others are more consistent with continuous star formation throughout the LMC’s early history (cf. Geha et al. 1998).

Despite their exquisite depth, the collected SFH solutions based on HST data are necessarily incomplete, simply because the HST field of view is vanishingly small compared to the solid angle subtended by the LMC: a full-coverage survey with ACS would require roughly 50,000 pointings. While we expect the older stellar populations to be well-mixed throughout the LMC, its stellar disk has a solid-body rotation curve out to roughly 4 kpc (van der Marel et al. 2002) and patterns imprinted by a spatially-variable star formation rate could persist in the LMC for several rotational periods (> 1 Gyr). Until now, a truly global analysis of the LMC’s SFH over its entire history has not been attempted.

We present a spatially-resolved solution for the global SFH of the LMC, based on a photometric catalog of over 20 million LMC stars. In Section 2, we briefly review our photometric catalog. In Section 3, we review our StarFISH synthetic CMD algorithm, and present some details on its application to the LMC data. We present our spatially-resolved map of the LMC’s SFH in Section 4, and discuss some of its implications in Section 5. The paper is summarized in Section 6.

2. THE MAGELLANIC CLOUDS PHOTOMETRIC SURVEY

The Magellanic Clouds Photometric Survey (MCPS; Zaritsky et al. 1997) was undertaken at the Las Campanas Observatory’s 1-meter Swope Telescope, between 1995 and 2000. It was a drift-scan survey using the Great Circle Camera (Zaritsky et al. 1996), covering $4^\circ \times 4.6^\circ$ in the Small Magellanic Cloud (Zaritsky et al. 2002), and $8.5^\circ \times 7.5^\circ$ in the LMC (Zaritsky et al. 2004). We obtained images with U , B , V and I filters, reaching a limiting magnitude between $V = 20$ and $V = 21$ mag, depending on the local degree of crowding in the images. For details on the data reduction, construction of

the photometric catalog, and quality assurance tests, see Zaritsky et al. (2002). The final LMC photometric catalog contains over 24 million objects, the vast majority of which are stars in the LMC. The photometry is presented in Figure 1 in the form of a “CMD triptych” (three Hess diagrams showing $U - B$ vs. B , $B - V$ vs. V , and $V - I$ vs. I).

We use both the $B - V$ and $V - I$ CMD planes in determining the best-fit SFH. StarFISH can easily be configured to operate simultaneously on any number of photometric planes (CMDs or two-color diagrams). Throughout this paper, when we are specifically discussing the present analysis, we will use the term “CMD pair” to describe the StarFISH analysis unit. However, when discussing StarFISH in general, we may use the more generic term “CMD”.

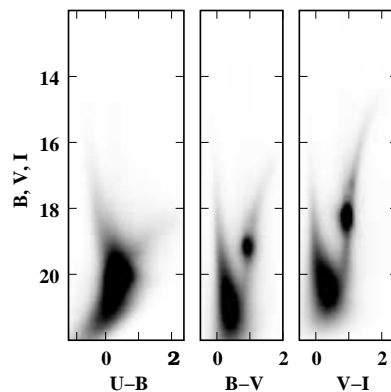


FIG. 1.— A “CMD triptych” illustrating our $UBVI$ photometry of ~ 20 million LMC stars. Each CMD panel is a Hess diagram whose pixel values are proportional to the number of stars in each pixel. The mixed populations evident in these CMDs represent a “fossil record” of a complex star-formation history in this galaxy.

3. DERIVING THE LMC’S STAR FORMATION HISTORY WITH STARFISH

StarFISH (Harris & Zaritsky 2001) is the software package that we created specifically for the synthetic-CMD SFH analysis of our MCPS data. However, we developed StarFISH with generality in mind, and to date it remains one of the few synthetic CMD packages that is publicly available for use by the astronomical community¹. We have already applied StarFISH to the MCPS catalog of the Small Magellanic Cloud (SMC, Harris & Zaritsky 2004), and the present analysis will be similar to that work; all important differences are noted in this Section.

StarFISH works by constructing a library of synthetic CMDs, each of which represents the predicted distribution in color and brightness for a stellar population of a particular age and metallicity. The library spans appropriate ranges in age and metallicity, so that any composite population can be generated as a linear sum of all the synthetic CMDs. The SFH of an observed stellar population is determined by minimizing the differences between the observed and model CMDs, via adjustment of the amplitudes. The collection of best-fit amplitude values – the proportional contribution of model stars of

¹ <http://ngala.as.arizona.edu/mcsurvey/>

each age and metallicity – represents the best-fit SFH of the observed stellar population.

3.1. The Isochrone Set

StarFISH can operate with any set of isochrones. We choose the latest isochrones from the Padua group (Girardi et al. 2002), because they provide a uniform set covering the relevant range of ages and metallicities, and include important post-red giant branch phases of stellar evolution (in particular, the red clump and asymptotic giant branch).

To prepare the isochrones for synthetic CMD construction, we first interpolate along each isochrone to increase the photometric resolution such that the photometric distance between adjacent points does not exceed 0.005 mag. This procedure ensures that when we populate the isochrones with artificial stars, there are no visible irregularities. Next, we determine the “occupation probability,” the relative probability of finding a star between points i and $(i + 1)$ along the isochrone for a given IMF. For a simple power-law IMF, the occupation probability is given by: $P = (M(i + 1)^\Gamma - M(i)^\Gamma)/\Gamma$ where $M(i)$ is the *initial* mass of a given isochronal point, and Γ is the power-law index (*i.e.*, $\Gamma = -1.35$ for a Salpeter IMF).

Finally, we adjust the age and metallicity resolution provided by the base isochrones to be appropriate for the observed data. For example, deep *HST* observations allow for much finer age resolution than shallow, ground-based data. This adjustment of the isochrone set involves subjective judgment by the user, but our rule of thumb is that we want a set of synthetic CMDs that each represent a unique distribution in the CMD plane. In other words, if a pair of isochrones is indistinguishable after adding photometric errors, then they should be combined into a single “group” that will be treated as one entity by the fitter. Similarly, if two adjacent isochrones have a detectable gap between them after adding photometric errors, then we use interpolation to insert an intermediate isochrone between them. StarFISH provides mechanisms for both grouping and interpolating to optimize the age and metallicity resolution. We find that the Padua isochrones provide a higher age resolution than our ground-based data warrant. Therefore, we join adjacent isochrones into age bins that span 0.2 dex, for $\log(\text{Age}) > 8.0$. For ages younger than 100 Myr, we increase the age interval to $\log(\text{Age})=0.3$ dex, resulting in bins with $\log(\text{Age})=7.7, 7.4, 7.1,$ and 6.8 . The wider age bins are necessitated by the steepness of the stellar IMF, which results in poorly-populated upper main sequences and supergiant sequences. We began the analysis with isochrones of three metallicities ($Z=0.001, Z=0.004,$ and $Z=0.008$), each of which is provided in the Padua set of isochrones. It quickly became apparent that our best-fit solutions would benefit from an additional metallicity bin, so we interpolated between the $Z=0.001$ and $Z=0.004$ isochrones to generate a fourth set of isochrones with $Z=0.0025$. The four metallicity bins are only used for the subset of isochrones with $\log(\text{Age}) \geq 8.0$. Providing multiple metallicity bins for younger ages proved to be counter-productive because the photometry of such stars is insensitive to metallicity, and so allowing metallicity variations for these ages only serves to inflate the fit uncertainties.

3.2. Interstellar Extinction

When attempting to model stellar populations in a galaxy’s diffuse field, it is important to match not only the mean extinction, but also the distribution of extinction values, as a function of age. Young stellar populations tend to have extinction values that are both larger on average and more widely distributed, than older stars. Indeed, Zaritsky et al. (2004) found that in the LMC the mean extinction among hot stars was four times larger than among cool stars, and that the dispersion in the hot-star extinction distributions tended to be larger. This difference likely arises because hot stars, which are typically younger than cool stars tend to be observed in the dustier environments in which stars form. In contrast, older stars have had time to drift away from their birthplaces, and so occupy more typical, lower-extinction environments.

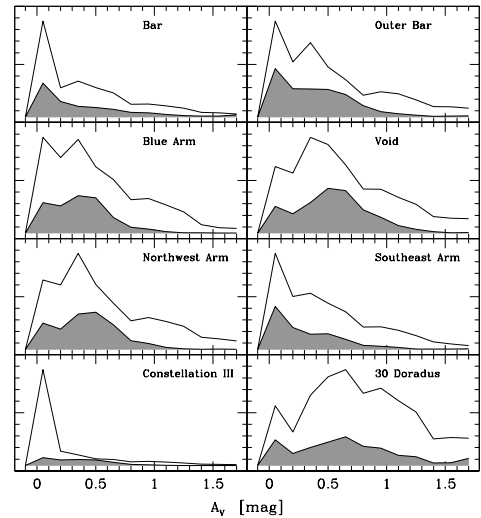


FIG. 2.— Extinction distributions for both hot (unshaded line) and cool (shaded line) star samples, for eight small subregions sampling various substructures in the LMC, as labeled in each panel. The plot illustrates the spatial variability in the extinction properties, as well as the wide distribution of extinction values within many of the regions. Derived negative extinctions arise due to photometric errors (see Zaritsky et al. 2004, for more details) and such values are set to $A_V = 0$.

To address these complications, we use distributions of extinction values that are either derived directly from the stars in the region being analyzed, or from stars in a different region with similar extinction properties. We refer the reader to (Zaritsky 1999; Zaritsky et al. 2004) for details. In Figure 2, we show some sample extinction distributions from different locations in the LMC, illustrating the degree to which extinction varies in this galaxy. While the extinction measurement for an individual star has significant uncertainty (0.1 to 0.2 mag; Zaritsky 1999), the distribution is derived from many stars in each region. In generating synthetic CMD libraries for determining the SFH for each of these regions, we draw extinction values randomly from the region’s own measured extinction distribution (assigning values from the hot-star distribution to synthetic stars younger than 10 Myr, cool-star values to synthetic stars older than 1 Gyr, and a linear interpolation between the hot

and cool star samples for synthetic stars with ages between 10 Myr and 1 Gyr). Thus, composite models constructed from the synthetic CMD library will accurately reflect the full range of the region’s extinction properties, including its mean value, dispersion, and distinct properties for its young and old components. We are able to use a given synthetic CMD library as the model for multiple regions, provided that the regions all share similar crowding and extinction properties. We do this because the generation of a synthetic CMD library is computationally expensive.

3.3. Photometric Errors

Before attempting to compare synthetic CMDs generated by StarFISH to observational CMDs, it is critical that the synthetic CMDs incorporate a realistic photometric error model that include random and systematic errors, and incompleteness fractions as a function of position in the CMDs. We perform artificial stars tests (ASTs) on the target images to construct robust, empirical error models that accurately reproduce the photometric properties of the real data. ASTs are especially important when the photometric errors are dominated by crowding, rather than photon statistics, as is the case for these data.

To perform such an AST, we inject artificial stars into the B , V and I images using the world coordinate system (right ascension and declination), which ensures that each artificial star appears in the same location with respect to the real stars in the field in all images. The artificial stars are placed in the image on a uniform grid, separated by ten times the radius of the point-spread function in V . This procedure ensures that each artificial star samples the crowding conditions of the original data image, with no interference from other artificial stars. We assign a V magnitude drawn from an exponential probability envelope that increases toward fainter magnitudes to better sample the faint end where errors and incompleteness change rapidly. B and I magnitudes are then assigned by drawing $B - V$ and $V - I$ colors randomly over the range covered by the real stellar populations. We perform several hundred AST iterations on each frame, randomly displacing the grid positions for each iteration, and reassigning the input photometry in each band.

We analyze the images with the artificial stars using the same DAOPhot photometry pipeline as previously, with the exception that we adopt the point-spread function model from the original analysis, rather than re-deriving it. We then record the $m_{input} - m_{recovered}$ difference in each band for the artificial stars. Artificial stars that are not detected by the pipeline analysis are used to determine the completeness. The ensemble of photometric Δm and completeness data provides the empirical error model we use to generate the synthetic CMDs.

Ideally, we would perform an independent AST for each LMC region. However, because the ASTs take several days to complete even on modern multicore computers, it is not practical to perform thousands of ASTs. Instead, we ran ASTs on the 17 LMC subregions listed in Table 1 that are carefully selected to be representative of the range of crowding conditions.

3.4. Deprojecting the LMC Disk

TABLE 1
THE ARTIFICIAL STARS TESTS

Subregion ^a	N_{\star}/\square'	$\langle A_V(hot) \rangle$ [mag]	$\langle A_V(cool) \rangle$ [mag]
DP	47.4	0.7	0.4
EP	69.4	0.7	0.4
CF	70.9	0.7	0.6
JC	77.7	0.6	0.5
GC	79.0	0.5	0.5
FP	94.3	0.5	0.4
EF	105.3	0.6	0.5
KC	105.9	0.7	0.5
LC	125.7	0.6	0.5
PN	131.2	0.4	0.4
MN	142.9	0.4	0.4
ON	145.9	0.25	0.4
NN	160.7	0.2	0.3
KF	174.6	0.5	0.4
HF	181.0	0.5	0.4
IF	186.7	0.5	0.4
OF	221.1	0.4	0.3
PD	174.6	0.7	0.5
PI	142.9	0.8	0.7
PM	131.2	0.5	0.5

^aEach two-letter code indicates the region’s position in our gridding of the LMC (see Figure 4).

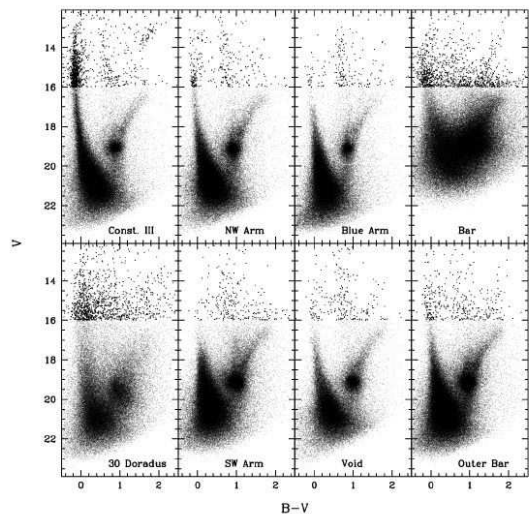


FIG. 3.— $B - V$ color-magnitude diagrams for the same eight LMC subregions as shown in Figure 2. Stars brighter than $V=16$ mag are shown with a larger point, to reveal the sparse distribution of these objects. The dramatic spatial variation in the stellar populations evident in this plot motivates a comprehensive, spatially-resolved analysis of the LMC’s SFH.

van der Marel & Cioni (2001) showed convincingly that the stellar populations in the LMC are distributed in a disk whose plane is inclined to the plane of the sky by 34.7° . Over the region covered by the MCPS, this inclination produces distance-modulus variations in the photometry larger than ± 0.1 mag. Prior to performing our StarFISH analysis, we deproject the measured photometry to a common distance modulus of 18.50 mag, using the geometry of the LMC disk reported by van der Marel et al.. We first transform each star’s right ascension and declination coordinates to a (R, Θ) polar coordinate system centered on the LMC ($5.483333^h, -69.5^\circ$). Then the line-of-sight distance to a star in the LMC plane, D in

kpc, is given by:

$$D = 50 + 0.873R \tan(i) \sin(\Theta - \Theta_0)$$

where R is the angular separation of the star from the LMC center (in degrees), Θ is the star’s azimuthal angle, and i and Θ_0 are the inclination and position angle of the LMC disk, as reported by van der Marel & Cioni. The value 0.873 represents the linear separation (in kpc) corresponding to an angular separation of one degree at a distance of 50 kpc. The photometric correction applied to the star is simply the difference between its in-disk distance modulus and the canonical LMC distance modulus of 18.50 mag.

3.5. Partitioning the Data

In Figure 3, we show $B - V$ CMDs for several subregions from our MCPS catalog. The stellar populations in these regions show clear differences that are rooted in variations of the SFH within the LMC. For example, the region labeled “Const. III” has a very prominent upper main sequence and a rich population of supergiants, indicating that this region has experienced a relatively large star formation rate over the past several tens of millions of years. The photometric error properties also vary substantially among these regions, driven primarily by variations in the stellar surface density. Variations in the stellar content and photometric error distributions motivate the spatial partitioning of our LMC catalog. The definition and characteristics of different regions are treated in more detail in §5.

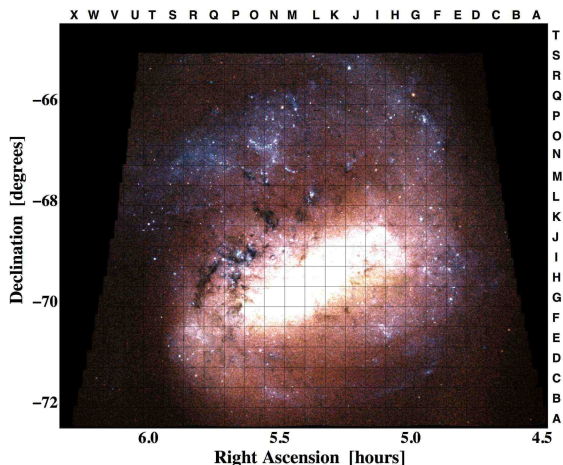


FIG. 4.— A stellar flux density map derived from our BVI photometry of the LMC. Overplotted on this map, we show our gridding strategy for reconstructing the spatially-resolved SFH. We divide the MCPS region into $24' \times 24'$ cells. Each of these cells may be further subdivided into a 2×2 grid of subregions, if the number of stars in the cell exceeds a threshold value. In practice, most of the top-level grid cells are subdivided in this way.

We divide the MCPS photometry using a grid and perform an independent StarFISH analysis on each region. This approach allows us to construct a spatially-resolved map of the LMC’s SFH. The geometry of the grid (in particular, the size of the grid cells) is driven by several considerations. To maximize our spatial resolution, we need to use the smallest possible regions. However, experience has taught us that StarFISH requires at least several thousand stars to avoid having acceptable χ^2 minima

that lie beyond the error bounds of each minima. This number does in detail depend on the stellar populations of the region, but the adopted number is generally applicable across our MCPS. We must also be mindful to control the spatial variations in the crowding interstellar extinction within each region.

Our gridding strategy is shown in Figure 4. The grid has a two-level hierarchy: we first divide the catalog into a uniform grid of 25×20 cells, each spanning approximately $24'$ in Right Ascension, and $24'$ in Declination. If any of these regions contain more than 25000 stars, then it is further subdivided into a 2×2 sub-grid. The final grid consists of 1380 subregions. We calculate an independent SFH solution for each of these regions, using a photometric error model drawn from one of our 17 ASTs that most closely matches the target region in stellar surface density. We also ensure that the extinction properties of the target region’s stars are well matched by the synthetic CMD library by comparing the hot and cool star extinction distributions as shown in Figure 2. If the extinction properties do not match, we generate a new synthetic CMD library using the region’s own measured extinction properties.

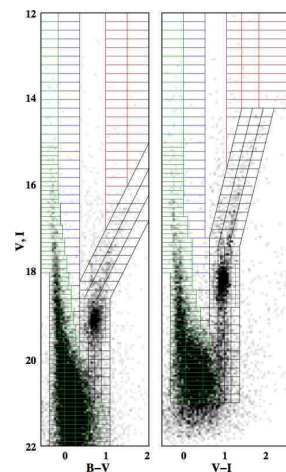


FIG. 5.— Gridding strategy for the $B - V$ and $V - I$ CMD planes, for our StarFISH analysis. The grid emphasizes the luminosity function of the main sequence (green boxes), the red giant branch and red clump (black boxes), and the red and blue supergiant sequences (red and blue boxes, respectively).

3.6. Finding the Best-Fit Star Formation History Model

StarFISH employs a downhill simplex (“amoeba”) algorithm to determine the best match between an observed CMD and a composite model CMD, formed from the linear combination of all CMDs in the synthetic library. Again, these synthetic CMDs each represent the predicted photometry for stars of a particular age and metallicity, given observational parameters (distance modulus, photometric errors and interstellar extinction properties) that are well-matched to the data. Through linear combination, we form a composite model that can represent any arbitrary mixture of ages and metallicities. The amplitude associated with each synthetic CMD in the composite model describes the SFH of the population (*i.e.*, its SFR and metallicity distribution as a function of time). These amplitudes form the multidimensional parameter space in which we search for the best fit SFH for

the observed stellar population. In the present analysis, we have synthetic CMD pairs covering 9 age bins and 4 metallicity bins, plus the 4 additional “young” age bins with no metallicity variation, for a total of 40 dimensions in the parameter space of the fitter.

The goodness-of-fit of any composite model CMD is evaluated by statistical comparison to the observed CMD. StarFISH can use a standard χ^2 fitting statistic, or the Lorentzian (Olsen 1999) or Poisson (Dolphin 2002) variants. We have found very little practical effect of this choice on the final best-fit determination, especially if the CMDs are well populated with stars (so that the inherent Poisson uncertainties of the CMD subregions approach the Gaussian shape assumed by the χ^2 statistic). For the present analysis, we choose the Poisson statistic. Whatever statistic is used, the fit determination involves dividing the CMD plane into small regions, and counting the number of stars present in each region in both the observed CMD and the composite model. The fitting statistic is minimized when the numbers of stars in the model’s CMD regions match those in the observed CMD regions most closely. For the present analysis, we use the CMD gridding strategy illustrated in Figure 5. This gridding strategy emphasizes features in the CMD pair that are sensitive to the SFH (such as the main sequence luminosity function, the red giant branch, and supergiant sequences), while ignoring regions that are likely dominated by contaminant populations.

The amoeba algorithm is initialized at a random position in the SFH parameter space, and it evaluates the fitting statistic for the composite model CMD at that location. It then takes a small step along each parameter space dimension (*i.e.*, varying each amplitude by a small amount while holding the others fixed) to determine the local gradient of the fitting statistic. It takes a step in the “downhill” direction, and then recomputes the local gradient. This procedure iterates until a minimum is found. As the amoeba descends through the parameter space, the deviations taken to determine the local gradient get smaller and smaller. When a minimum is found, the amoeba is reset to another random position within the SFH space, to ensure that it still returns to the same minimum position. In addition, we have added a feature in which “off-axis” directions are probed for further downhill gradient opportunities. The stock amoeba algorithm only searches along each parameter dimension when evaluating the gradient; thus it can wrongly conclude that a minimum has been reached if multiple amplitudes need to be simultaneously varied to achieve a better fit.

The SFH is often expressed as the SFR as a function of time. However, StarFISH does not directly determine the SFRs; fundamentally, it determines the number of stars *present in the CMD* as a function of age and metallicity. In order to translate this to the SFR, we need to perform a number of renormalizations. First, we need to convert from the number of stars that are observed in the CMD, to the total number of stars present in the observed region. This is essentially a completeness correction, accounting for those stars that are too faint to be observed. This correction is a strong function of age, and depends on an assumed IMF. Once we have the total number of stars present, we need an additional correction to get the total number of stars that were originally

formed. This is a correction for the fraction of the stellar population that has evolved away to non-luminous end-states, and it is also a strong function of age. For example, we can observe nearly the entire stellar population if it is a few Myr old, but if it is 12 Gyr old, then a significant fraction of the stellar population no longer exists, and we must account for this if we want to infer the number of stars formed 12 Gyr ago, from the number of 12 Gyr stars that remain. Once we have the total number of stars formed at each age, we multiply by the average stellar mass (given an IMF), and divide by the time interval covered by the age bin to get the SFR in M_{\odot}/yr .

A more detailed discussion of the uncertainties in the method, tests of the SFH reconstruction with known populations, comparison of observed and synthetic CMDs, and the dependence of χ^2 on undetermined parameters such as binary fraction are presented by Harris & Zaritsky (2001, 2004). Unless otherwise specified, we have adopted the same parameters as adopted in Harris & Zaritsky (2004).

3.7. Estimating Fit Uncertainties

Once the minimum of the fitting statistic has been determined, StarFISH evaluates the fit uncertainties by exploring the parameter space in the vicinity of this best-fit location. Some SFH methods simply rely on the statistics of the points evaluated on the way to reaching the minimum to estimate the parameter uncertainties. However, we find that a systematic exploration of the parameter space surrounding the best-fit location does a much better job of determining realistic uncertainties. With 40 parameters, it is not possible to completely explore the parameter space, but we have developed a multi-step procedure that allows us to examine the independent variance of each amplitude, the covariance of pairs of amplitudes, and the general covariance of all amplitudes. In all cases, we step away from the best-fit parameter space location along a single parameter-space direction until the fit worsens to the point that we have reached the 68% (1σ) confidence interval. Along the way, we keep track of the maximum deviation of each amplitude from its best-fit value that remains within the 68% confidence interval. In the first phase of the procedure, we determine the independent variance of each amplitude by both increasing and decreasing each amplitude while holding all others fixed, until the 68% confidence limit is reached. In the second phase, we explore the pairwise covariance of adjacent amplitudes. For each pair of adjacent amplitudes, we allow them to vary against each other while all other amplitudes are held fixed, until the 68% confidence limit is reached. This procedure is done both in age and metallicity. In the third phase, we explore general covariance by choosing a completely random parameter space direction and stepping away from the best-fit location until the 68% confidence limit is reached. The random-direction search is repeated 30,000 times in an attempt to adequately sample the topology of the local parameter space. Formally, 30,000 iterations is grossly inadequate to cover a 40-dimensional parameter space. However, we find that the local topology tends to be sufficiently smooth that exploring the independent variance of each amplitude, as well as the pairwise variance of all pairs of amplitudes, is usually enough to provide a reasonable

picture of the fit uncertainties. In other words, it is rare that our phase 3 explorations result in a further increase of the confidence intervals over and above what phases 1 and 2 determined.

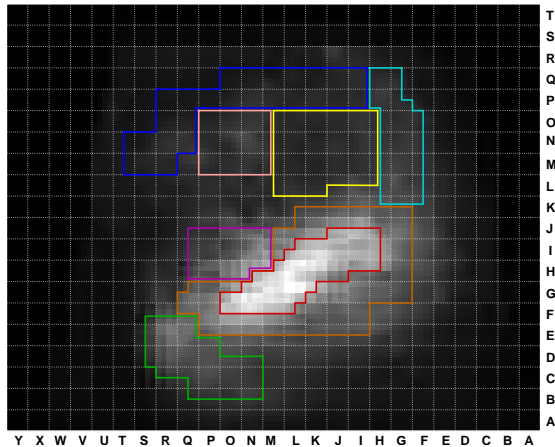


FIG. 6.— A star-count map of the LMC, in which the pixel value in each grid region is proportional to the number of stars present in that region. The map highlights several collections of regions for which we will examine the SFH in detail: the LMC Bar (red), the Outer Bar (orange), 30 Doradus (magenta), the “Southeast Arm” (green), the “Northwest Arm” (cyan), the “Blue Arm” (blue), Constellation III (pink), and the “Northwest Void” (yellow).

3.8. Using HST Results to Constrain the Bar’s Ancient SFH

Our MCPS photometry is relatively shallow, and barely reaches the ancient MSTO which occurs around $V = 21$ mag for stars in the LMC. In the crowded bar regions, our photometry is significantly shallower, perhaps a magnitude brighter than the old MSTO. Because most of the age information for old stellar populations is provided by the MSTO, it is difficult to extract the early SFH of the LMC from our MCPS photometry, especially for the bar region. For this reason, we restrict StarFISH to fitting a single age bin covering all ages older than 4 Gyr in the bar region.

Within the bar (see Figure 6), we use the information for old ages from published SFH solutions based on deep HST data, as mentioned in Section 1. The HST fields, while tiny, should sample the old SFH fairly because orbital mixing will have erased any spatial variation. The derived SFH in the three published studies that used deep HST imaging of LMC bar fields (Olsen 1999; Holtzman et al. 1999; Smecker-Hane et al. 2002) agree remarkably well (see Figure 7). Each finds an initial epoch of star formation that is extinguished by 10 Gyr ago, and then resumes about 5 Gyr ago. The shape of the Olsen solution is somewhat different than the other two, but this disagreement is likely due to the lower time resolution and younger age limit used in that study. We adopt a consensus SFH based on these HST results to represent the portion of our SFH solutions older than 4 Gyr. In other words, we use StarFISH to determine the total number of stars older than 4 Gyr in a given LMC bar subregion, but those stars are distributed in age according to the consensus HST SFH solution.

To check the validity of our HST-anchored solutions, we performed an alternative set of solutions for all 1380

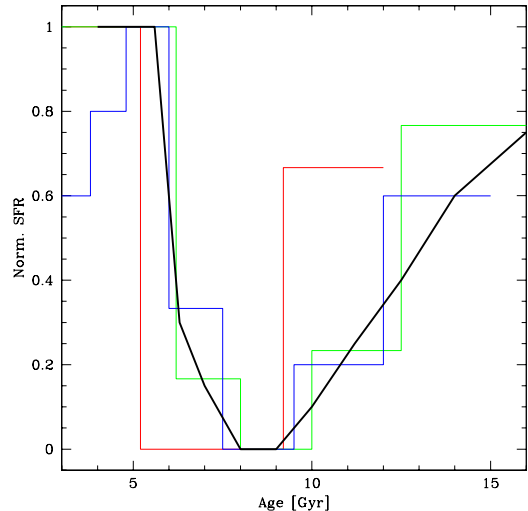


FIG. 7.— The SFH solutions for ages > 4 Gyr from three independent studies of the LMC Bar, using HST imaging. The solutions are: Olsen (1999) (red line), Holtzman et al. (1999) (green line), and Smecker-Hane et al. (2002) (blue line). The three solutions show remarkable agreement, especially when considering that Olsen chose a relatively young age limit of 10 Gyr. In the present analysis, we will require that our SFH solutions conform to the black curve for ages older than 4 Gyr. In this way, we rely on the deep HST imaging to supplement our relatively shallow ground-based data.

subregions in the LMC map, in which we did not use the HST results to constrain the old SFH. In this case, we simply extend our $\Delta \log(t) = 0.2$ age-binning strategy to include bins with $\log(t) = 9.8, 10.0$ and 10.2 . We find that this alternative set of solutions produces obvious spatially-dependent artifacts in the early panels of the SFH map. However, for ages ≤ 4 Gyr, the SFH map is indistinguishable from that of the HST-anchored solutions. Because of the artifacts present in the early bins, we will restrict ourselves to the set of solutions constrained to match the HST results for ages older than 4 Gyr for the remainder of the paper, unless otherwise noted.

4. RESULTS: A MAP OF THE LMC’S STAR FORMATION HISTORY

We have performed SFH solutions for nearly 1400 LMC subregions. Putting all of these solutions together allows us to construct a map of the total SFH of the LMC, which is shown in Figure 8. The map shows the entire MCPS survey region covering the central $8^\circ \times 8^\circ$ of the LMC. Each panel shows the star formation rate for a particular time-step in the LMC’s history. The pixel values are proportional to the SFR at that time, color-coded for the metallicity. Because the time interval covered by each panel increases logarithmically with time, displaying the star formation rate does not provide an intuitive grasp of the age at which most stars were formed. We therefore also provide an alternative view of the SFH map, in which the pixel values are proportional to the total stellar mass formed in each timestep (Figure 9). In this view, it is apparent that a significant portion of the LMC’s stellar mass had been assembled by 10 Gyr ago.

Figures 8 and 9 show that the LMC’s SFH has rich structure both spatially and temporally. Due to dynamical mixing and the longer time intervals covered, the older time bins are generally spatially and temporally

TABLE 2
THE STAR FORMATION HISTORY OF THE LMC

	Z = 0.008			Z = 0.004			Z = 0.0025			Z = 0.001		
log(age)	SFR	SFR _l	SFR _u	SFR	SFR _l	SFR _u	SFR	SFR _l	SFR _u	SFR	SFR _l	SFR _u
	Region AA (04 ^h 31 ^m , -72° 17')											
10.20	0	0	5	0	0	7	0	0	12	39	28	53
10.00	0	0	4	0	0	8	0	0	13	24	13	37
9.80	0	0	5	0	0	8	0	0	14	17	5	31
9.60	0	0	6	0	0	11	0	0	15	0	0	12
9.40	0	0	12	67	50	87	191	174	210	14	0	28
9.20	0	0	16	0	0	12	0	0	13	0	0	11
9.00	4	0	17	0	0	10	0	0	8	0	0	8
8.80	7	0	21	0	0	11	0	0	13	17	7	30
8.60	0	0	12	11	0	28	0	0	16	0	0	11
8.40	0	0	9	0	0	9	0	0	10	0	0	11
8.20	0	0	9	0	0	14	0	0	18	10	0	32
8.00	0	0	12	0	0	19	9	0	37	5	0	30
7.70	8	0	27	0	0	0	0	0	0	0	0	0
7.40	12	0	38	0	0	0	0	0	0	0	0	0
7.10	0	0	28	0	0	0	0	0	0	0	0	0
6.80	0	0	46	0	0	0	0	0	0	0	0	0

NOTE. — The complete version of this table is in the electronic edition of the Journal. The printed edition contains only a sample. SFRs are in units of $10^{-6} M_{\odot} \text{yr}^{-1}$.

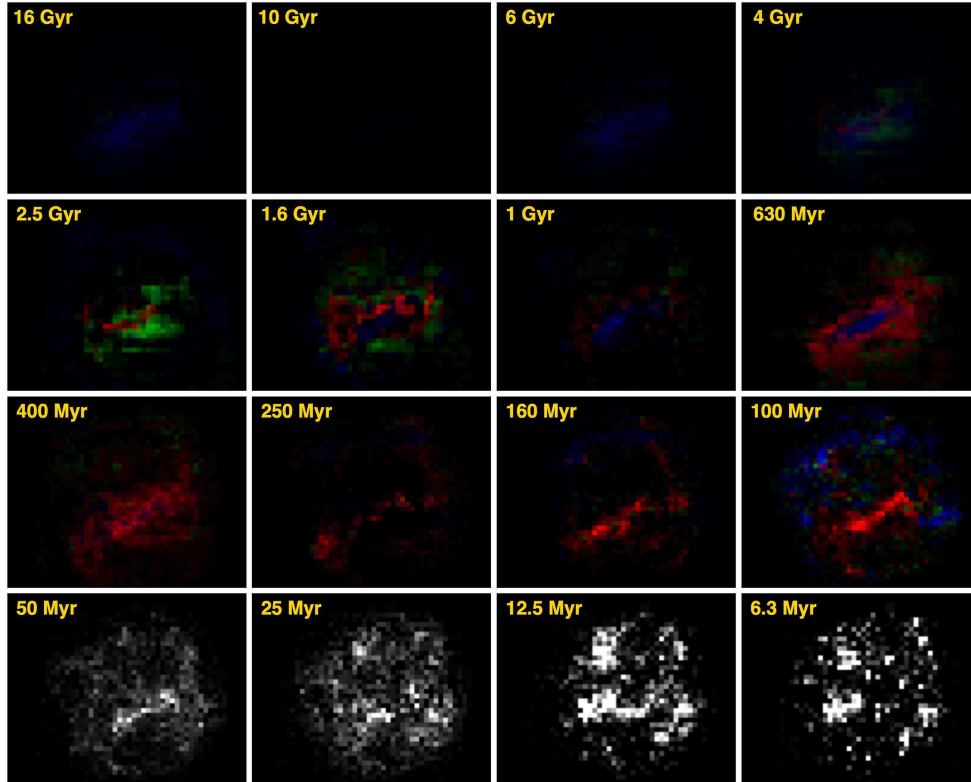


FIG. 8.— The map of the LMC’s SFH, based on the StarFISH solutions for over 1300 subregions. The pixel value for each region is proportional to the star formation rate at that location, color coded for the metallicity (with Z=0.001 shown as blue, Z=0.004 shown as green, and Z=0.008 shown as red). There is no color-coding for $\log(\text{Age}) < 8.0$, because the fitter is not given multiple metallicity bins for these young ages.

smoother than the younger bins. In the youngest bins, we can associate peaks in the map with well-known star-forming regions in the LMC. For example, the concentration to the left of center and slightly below is 30 Doradus, and the concentration directly above 30 Doradus is LMC Constellation III.

In Figure 10, we show the spatial correlation of the young (Age ≤ 12.5 Myr) star-formation activity as derived from our analysis and the $H\alpha$ emission in the LMC from the Magellanic Clouds Emission Line Survey (Points 2008). As expected, $H\alpha$ flux and recent star-formation activity correlate because both quantities are causally linked to the presence of young stars. However, the correlation is not perfect: there are regions that have large $H\alpha$ flux, but show little or no signal in the recent SFH map and there are hotspots in the recent SFH map that show little or no $H\alpha$ flux. Some of the non-correlation can be understood from the fact that $H\alpha$ flux is not purely a tracer of star formation activity; it requires *both* recent star formation *and* the presence of significant amounts of hydrogen gas. For example, the large region of recent star-formation activity visible in the northern disk in Figure 10 is the Constellation III region. We know from tracers of the interstellar medium (such as H I and $8\mu\text{m}$ emission) that Constellation III is embedded in a cavity from which the gas has been evacuated (Kim et al. 1998; Meixner et al. 2006), making $H\alpha$ emission here impossible. On the other hand, there are many regions in Figure 10 in which we see a localized peak in the $H\alpha$ flux with no corresponding peak in the recent SFH map. To understand these cases, we point to the different spatial resolutions of the SFH map and the $H\alpha$ image. A small cluster or OB association can lead to a bright HII region with only a few photoionizing stars. However, a small handful of young stars will not be statistically significant enough to sway the SFH solution.

The LMC bar has had a distinct SFH from that of the general LMC disk. The bar dominates in some of the panels in Figure 8 (16 Gyr, 6 Gyr, 630 Myr, 400 Myr, 160 Myr), but is largely absent from others (1.6 Gyr, 250 Myr, 25 Myr, 12.5 Myr, 6.3 Myr). At 2.5 Gyr, there is centrally-concentrated activity in the map, but unlike that seen in the younger panels, its structure does not closely resemble the current contours of the bar.

At 160 and 100 Myr, there is a “Northern Arm” feature composed of low-metallicity star-formation activity in the outskirts of the northern LMC disk. The possibility of recent low-metallicity star formation activity that is coherent across several kpc in the LMC disk is intriguing. However, metallicity variations become photometrically degenerate for younger stellar populations, and in fact we chose to eliminate metallicity variations for ages younger than 100 Myr in order to avoid these degeneracies. What features in the CMD are driving the fitter to conclude that the northern outskirts of the LMC disk saw low-metallicity star formation 100 Myr ago? The likely answer is that the mean color of the faint main sequence is slightly bluer in these regions than in other regions. Overplotting the $Z=0.001$ and $Z=0.008$ isochrones on a CMD for an age of 100 Myr shows that the upper main sequences are nearly coincident, but toward fainter magnitudes, the metal-rich isochrone shows a deviation to the red. By $M_V=2.5$ mag ($V=21$ mag for the LMC),

the deviation in $(B - V)$ is almost 0.2 mag. While the supergiant sequences in the isochrones show substantial differences between $Z=0.001$ and $Z=0.008$, these evolutionary stages are so poorly populated compared to the main sequence that they do not carry much weight in determining the fit. As a test, we selected two adjacent regions from the LMC SFH map that show similar activity in the 100 Myr panel (with one dominated by $Z=0.001$ stars, and the other by $Z=0.008$ stars). Indeed, the faint main sequence stars in the metal-poor region are 0.1 mag bluer, on average, than the stars in the metal-rich region. To the extent that the faint-end color variations are considered real, metallicity variations are one plausible, but not unique, explanation for them. Spectroscopic follow-up is needed to confirm these apparent metallicity variations among stars aged 100–160 Myr in our map.

5. DISCUSSION

5.1. The LMC’s Total Star Formation History

Combining the SFH solutions from all 1380 LMC regions, we construct the SFH for the entire LMC (Figure 11). In the Figure we also show an alternative representation of the SFH: the cumulative stellar mass formed in the LMC as a function of time, which shows that half of the LMC’s stellar mass was assembled 5 Gyr ago. Note that the stellar mass in this plot includes the initial mass of all stars formed, including stars that have already evolved to non-luminous end-states and returned large fractions of their mass to the interstellar medium.

One of the most dramatic features in the global SFH solution is the quiescent epoch spanning roughly 5–12 Gyr ago. The presence of this quiescent epoch is imposed by our decision to tie the old SFH to the HST results (see Figure 7). However, the quiescent epoch is also present in the total SFH derived from the alternate set of solutions that were *not* tied to the HST results, so it is not an artifact of the adopted HST solutions, but a robust feature of the LMC’s history, reflected in both its cluster and field populations. After an initial epoch of star formation, the LMC all but ceased forming stars, sustaining an average star formation rate of only $0.02 M_\odot \text{yr}^{-1}$ over the interval between 12 and 5 Gyr. Following the quiescent epoch, star formation resumed throughout the galaxy, and it has remained active ever since, with an average rate of $0.2 M_\odot \text{yr}^{-1}$. It is tempting to speculate that something dramatic happened to the LMC 5 Gyr ago to precipitate the global resumption of star formation, such as a merger with a gas-rich dwarf galaxy, or a gravitational interaction with the Milky Way.

The total SFH solution in Figure 11 shows episodes of enhanced star-formation activity at 12 Myr, 100 Myr, 500 Myr, and 2 Gyr ago. These episodes represent deviations from the long-term average star formation rate of up to a factor of two. However, as our age resolution becomes coarser with increasing age, ever larger deviations in the star formation rate can remain undetected if they occurred on a sufficiently short timescale.

As noted by many for at least 20 years (cf. van den Bergh 1981; Nikolaev & Weinberg 2000), the peaks in the SFR did not occur uniformly throughout the LMC (Figure 8) and our study enables a detailed temporal and morphological study of this behavior. For example, the activity at 100 Myr is concentrated along the present-day bar, while the activity at 2 Gyr is centrally concentrated

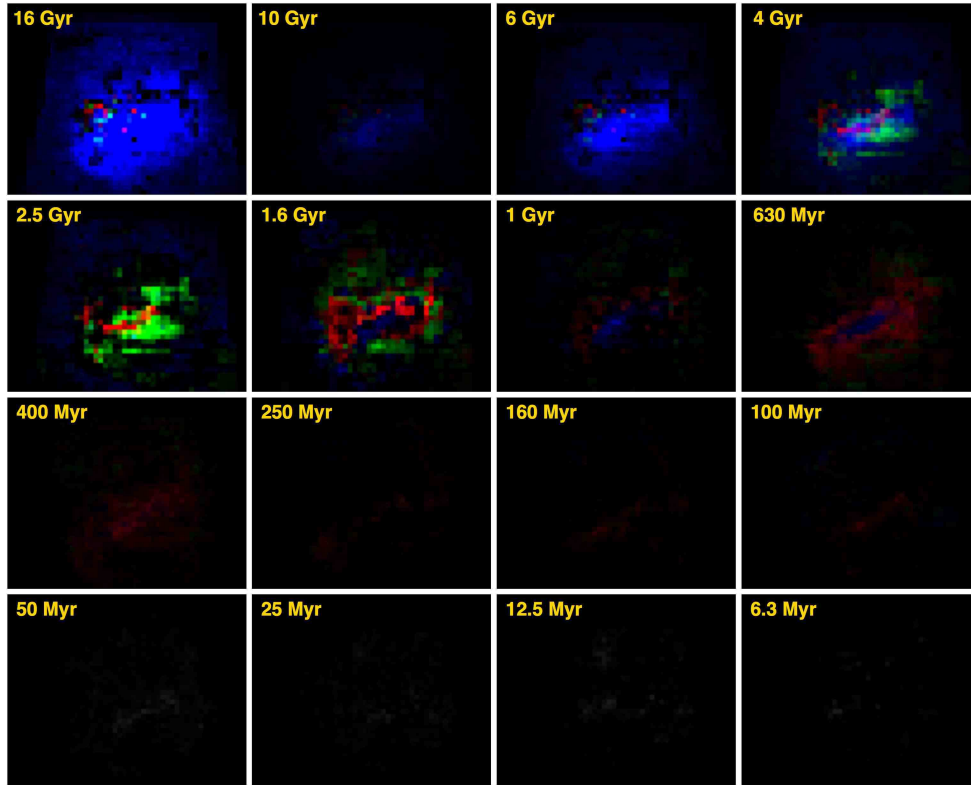


FIG. 9.— The map of the LMC’s SFH, based on the StarFISH solutions for over 1300 subregions. In this version of the map, the pixel values are proportional to the total stellar mass formed, rather than the star formation rate.

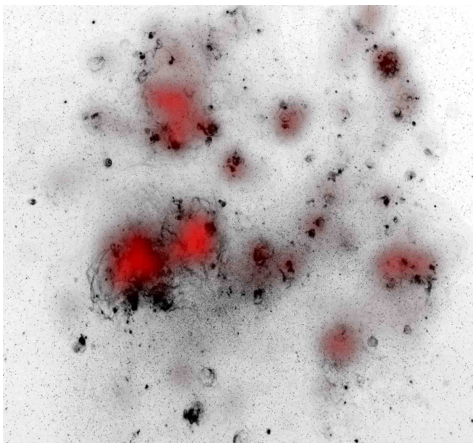


FIG. 10.— The correlation of the recent (Age < 12.5 Myr) star formation activity in the LMC based on our analysis, with the H α image of the LMC from the Magellanic Clouds Emission Line Survey (MCELS) (Points 2008).

and does not follow the contours of the present-day bar. We examine the SFH solutions of eight localized features in the LMC, some of which are well-known structures (such as the bar), and others which are only distinguishable in our SFH map. The eight regions are outlined in Figure 6.

5.1.1. The LMC Bar

The LMC bar is an enigmatic cigar-shaped structure that dominates optical images of the LMC. This feature is often thought of as a massive dynamical bar, which are common at the centers of spiral galaxies. However, for a number of reasons, it is difficult to understand the LMC bar as a dynamical structure embedded in the LMC disk.

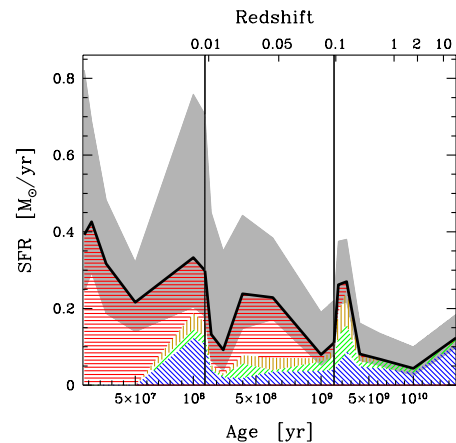


FIG. 11.— The total SFH of the LMC, computed by summing over all 1376 regions covering the MCPS survey region. The time axis is shown with a linear scale that is broken into three segments: the left panel covers ~ 100 Myr, the middle panel covers ~ 1 Gyr, and the right panel covers ~ 14 Gyr. The best-fit star formation rate (SFR) as a function of age is shown with a thick black line; the uncertainty on the fit (including covariance between age bins) is shown as a grey shaded envelope. The distribution of metallicity at each age is shown by the mix of colors below the SFR line ($Z=0.001$ in blue and downward sloping; $Z=0.0025$ in green and upward sloping; $Z=0.004$ in orange and vertical; $Z=0.008$ in red and horizontal).

Most dramatically, the bar is absent in images that trace the interstellar medium of the LMC, such as HI (Kim et al. 1998), H α (Points 2008), CO (Mizuno et al. 2001), or $8\mu\text{m}$ and $24\mu\text{m}$ emission (Meixner et al. 2006). A dynamical bar is the manifestation of a gravitational instability in a galaxy disk, and should therefore sweep all

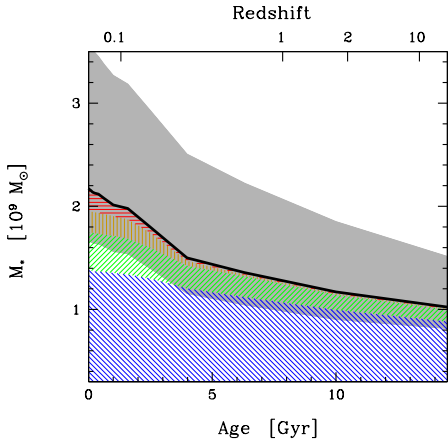


FIG. 12.— The cumulative stellar mass formed in the the LMC. Shading and colors same as in previous Figures although the time axis is now linear.

types of matter – stars, gas and dust. Another, perhaps related, source of ambiguity is that present-day star formation is not concentrated in the bar, as often happens in barred spiral galaxies. Dynamical bar structures funnel gas and dust into the center of the galaxy (Mackey & Gilmore 2004), leading to a nuclear starburst (*e.g.* Schinnerer et al. 2006). In the case of the LMC, the most active star-forming regions in the LMC (including 30 Doradus) lie well outside the bar. Lastly, differential distance measurements to the bar and disk suggest that the bar is closer to us by as much as 0.5 kpc (Nikolaev et al. 2004). The complicated interaction history, both with the SMC and our Galaxy, provide many opportunities for complicated dynamical effects and distorted morphological features (*cf.* Staveley-Smith et al. 2003).

Zaritsky (2004) proposed that the LMC bar may actually be a bulge population that is half-obscured by the optically-thick disk of the LMC. This hypothesis can explain many of the bar’s properties, but the required disk opacity is challenged by extinction measurements in the LMC, by the distribution of stellar flux in infrared images, which are far less obscured by dust, and by the stellar kinematics, which are normal (Cole et al. 2005).

These mysteries motivate us to look for answers in the bar’s SFH. In the SFH map of the entire LMC (Figure 8), the bar shows intermittent periods of activity and quiescence throughout the LMC’s history, as has been noted previously (Hardy et al. 1984; Smecker-Hane et al. 2002). It had particularly active episodes 5 Gyr, 500 Myr, and 100 Myr ago. At other times (*e.g.*, 2.5 Gyr and 12 Myr), there is significant star-formation activity in the bar, but the distribution of the star-formation activity at these ages does not match the present-day structure of the bar. At 2.5 Gyr, the centrally-concentrated activity is oriented along a position angle that is closer to the East-West direction than the present-day bar. This offset may mean that the 2.5 Gyr old stellar population has little to do with the bar. Similarly, the activity at 12 Myr is dominated by 30 Doradus and the Constellation III region, which are not related to the bar. While there is corresponding activity near the center of the bar region, it does not pervade the entire bar, as it does at 100 Myr.

The integrated SFHs of the inner and outer bar regions are shown in Figure 13, although given the ques-

tions about the nature of the bar defining the bar population is difficult (*cf.* Cole et al. 2005). There is striking coherence in the timing of star-formation events among the bar, arm (Figure 14), and void (Figure 18) regions. Whatever its nature, the bar has been an integral part of the LMC for most of its history. The biggest distinguishing features of the bar’s SFH are that its quiescent periods at 250 Myr and 1 Gyr are relatively deeper than in other parts of the LMC and the peak in the SFR at 5 Gyr is relatively stronger.

5.1.2. The LMC Arms

While the LMC is clearly a disk galaxy, the evidence for spiral arms in the LMC that are the result of a spiral density wave is tenuous at best. In this Section, we refer to the LMC’s “arms” as the structures extending off the ends of the LMC bar that are morphologically similar to spiral arms (see Figure 6), without implying that there is necessarily a spiral density wave in the LMC’s disk.

The integrated SFHs of the northwest and southeast LMC arm regions (Figure 14) are remarkably different. The northwest arm region had very little star-formation activity prior to 5 Gyr ago, and it also lacks the quiescent period at 1 Gyr seen in most other regions. The activity at 100 Myr seen in most other regions also seems to be suppressed here, and its recent SFH is characterized by a steady increase in the SFR since 100 Myr ago. In the southeast arm, we see one of the strongest signatures of the short-term burst of activity at 2.5 Gyr. Most remarkably, the recent star-formation activity in the southeast arm peaked 600 Myr ago and has been declining since. These differences suggest that these structures are probably not the sole result of a spiral density wave in the LMC disk for which we would expect to see more symmetry.

5.1.3. The “Blue Arm”

We define the region we call the “blue arm” to enclose the coherent low-metallicity star-formation activity in the LMC’s northern disk 100 Myr ago (Figure 8). In Section 4, we argued that the low metallicity of this feature should be treated with some skepticism because metallicity variations produce only subtle differences along the main sequence of younger stellar populations. While we still recommend this skepticism, it is interesting to note that the integrated SFH of the blue arm region shows that the metallicity here has been relatively low throughout its history.

Even if the low metallicity in this region is a photometric artifact, the blue arm is still remarkable as the remains of a major star formation event in the outer disk of the LMC 100–160 Myr ago. The total stellar mass formed during this event was roughly a factor of five greater than the stellar mass formed in Constellation III or 30 Doradus. The blue arm is less spatially concentrated than these younger structures, probably due to dynamical mixing during the 100 Myr since its formation.

5.1.4. Constellation III

In Harris & Zaritsky (2008), we performed a detailed analysis of the SFH of Constellation III, based on the same MCPS photometry used here, but concentrating

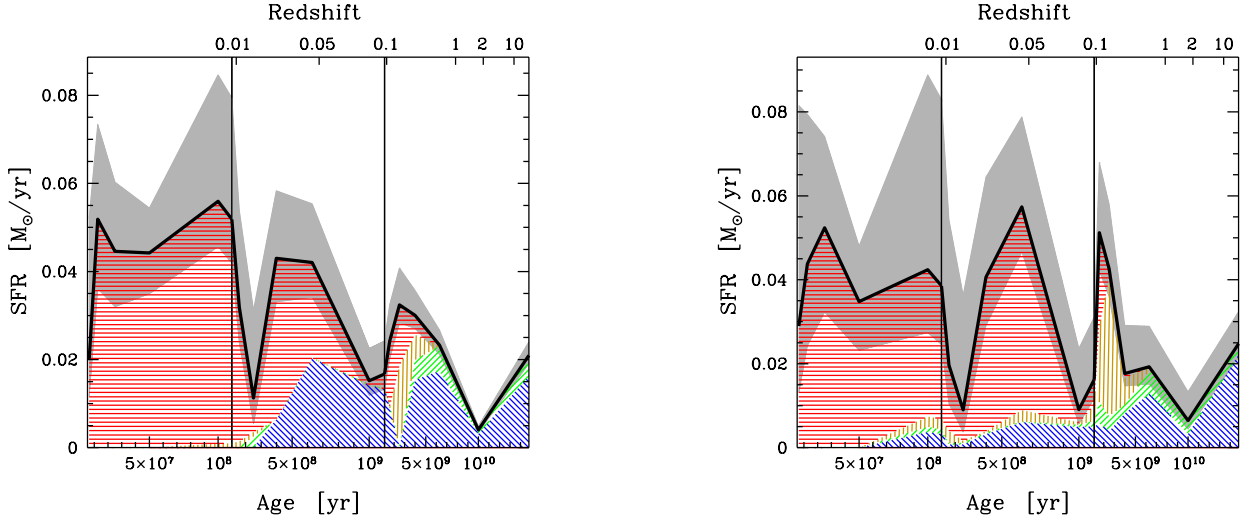


FIG. 13.— The integrated SFH solutions for the LMC Bar (left) and Outer Bar (right) regions. The shading and colors are the same as in Figure 11.

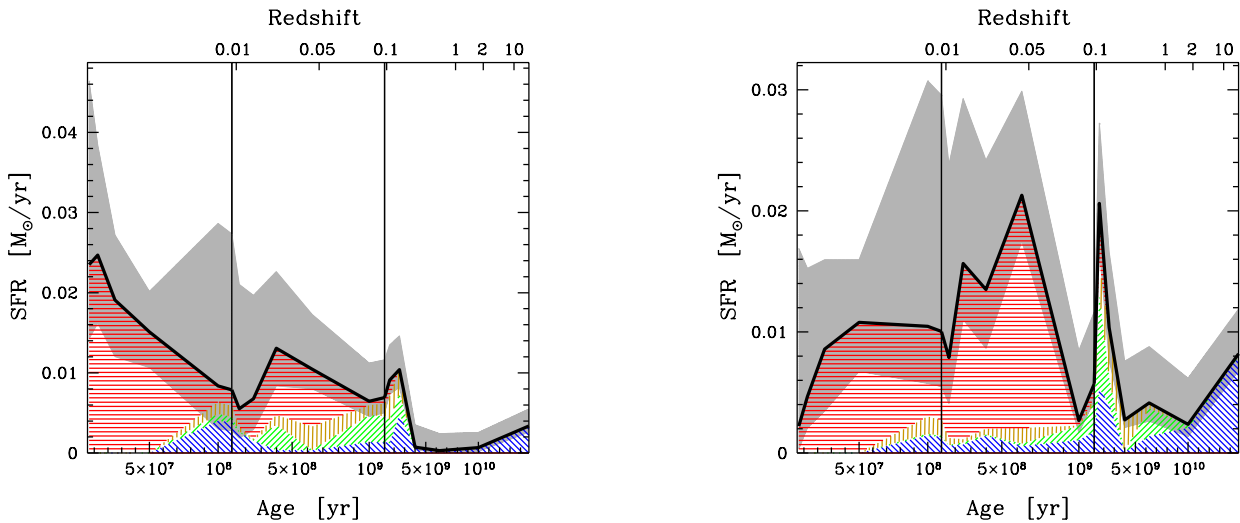


FIG. 14.— The integrated SFH solutions for the Northwest Arm (left) and the Southeast Arm (right) regions. The shading and colors are the same as in Figure 11.

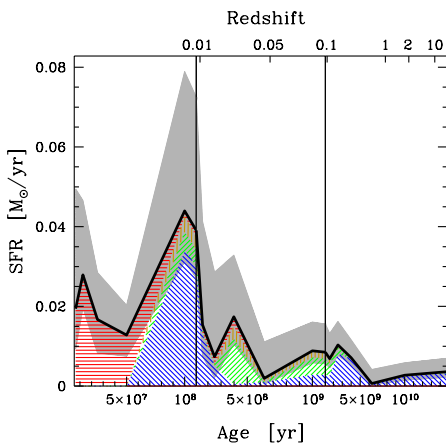


FIG. 15.— The integrated SFH solution for the Blue Arm region. The shading and colors are the same as in Figure 11.

on the photometry of the region's abundant supergiant population to provide higher temporal and spatial resolution in the recent SFH. For example, we were able to distinguish two bursts of activity at 10 Myr and 30 Myr, whereas in the present analysis (Figure 16), we are only able to resolve a single recent burst. The solution in Figure 16 is entirely consistent with the analysis of Harris & Zaritsky (2008). The SFH of this region reveals that this is a relatively young structure in the LMC disk: prior to 50 Myr ago, the SFH of this region is indistinguishable from that of the void region (Figure 18).

5.1.5. 30 Doradus

30 Doradus is one of the most active star-forming regions in the local universe, and as such there is a lot of interest in understanding the conditions that led to its formation. Clues might be present in the detailed, spatially-resolved reconstruction of its SFH. The integrated SFH of 30 Doradus (Figure 17) reveals little more

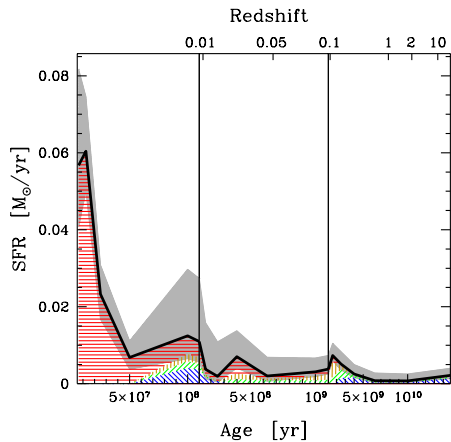


FIG. 16.— The integrated SFH solution for the Constellation III region. The shading and colors are the same as in Figure 11.

than the quintessential feature of 30 Doradus: that it is a hotspot of very recent star-formation activity. Figure 8 shows that the 30 Doradus region is not distinguishable in the SFH map until about 12 Myr ago, implying that, like Constellation III, 30 Doradus formed only very recently. A more targeted analysis that can achieve a higher age resolution for recent ages (such as we have already done for Constellation III; Harris & Zaritsky 2008) might reveal more about the evolution of this important star-forming region but is beyond the scope of this study.

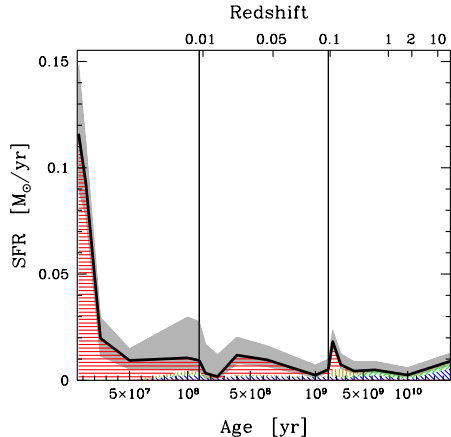


FIG. 17.— The integrated SFH solution for the 30 Doradus region. The shading and colors are the same as in Figure 11.

5.1.6. The “Northwest Void”

There is a large region in the northwestern disk that shows no enhanced star formation activity at any epoch (see Figure 8). We refer to the region as the “northwest void”. However, we see that the integrated SFH of the northwest void (Figure 18) closely resembles the total integrated SFH of the entire LMC (Figure 11). In some sense, then, the void offers a look at the LMC’s typical stellar population, unpolluted by recent localized deviations from the average behavior.

5.2. Imprints of the LMC’s Interaction History

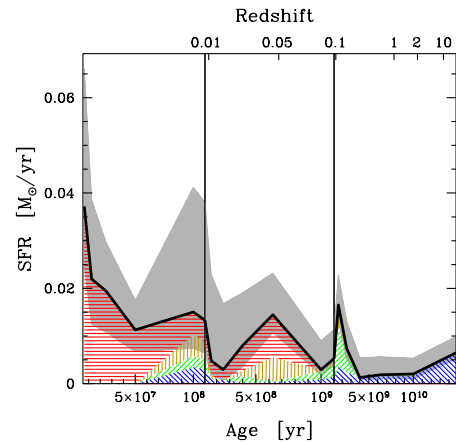


FIG. 18.— The integrated SFH solution for the Northwest Void region. The shading and colors are the same as in Figure 11.

Until recently, the Magellanic Clouds were widely regarded as long-term satellite galaxies of the Milky Way, in decaying orbits that would eventually lead to their consumption by our Galaxy (Gardiner et al. 1994; Bekki et al. 2004). In Harris & Zaritsky (2004) and Zaritsky & Harris (2004), we used this context to interpret the SFH solution for the SMC; in particular, we noted coincidences between peaks in the SMC’s SFR and past perigalactic interactions with the LMC and Milky Way. Among these coincident peaks, the most striking was one that occurred 2.5 Gyr ago, coinciding with what was previously identified as the time of a triple-interaction among the LMC, SMC, and Milky Way. We see the same peak in the present analysis of the LMC’s SFH, further evidence for a major interaction at that time in their shared history.

However, the idea that the Magellanic Clouds have always been satellites of the Milky Way has been seriously challenged by a new measurement of the LMC’s proper motion, using differential astrometry against background quasars from HST images (Kallivayalil et al. 2006; Besla et al. 2007). The new proper motion is twice as large as previous measurements. With this large a proper motion, a closed orbit for the LMC around the Milky Way is possible only if the true mass of the Milky Way is larger than current measurements suggest. In fact, the orbital reconstructions in Besla et al. (2007) suggest that the LMC may not even be bound to the Local Group potential. In their best-fit reconstruction, the LMC was over a Mpc away from the Milky Way 5 Gyr ago.

The new proper motion measurement challenges the idea that the Clouds are satellites of the Milky Way, but its impact on their gravitational relationship with each other is much less clear. Given the uncertainties still present in the SMC proper motion measurement, it is still possible that the Clouds are a long-term binary galaxy. Assuming that past interactions between the Clouds trigger enhanced star formation activity in both galaxies, we search for evidence of past interactions between the Clouds by looking for coincident peaks in their SFH solutions. The SMC’s integrated SFH solution is shown in Figure 19, adapted from Harris & Zaritsky (2004). Comparing the SMC’s solution to that of the LMC (Figure 11), we do see two coincident peaks at 400 Myr and 2.5 Gyr which suggest that the Clouds

may indeed have a common interaction history that extends back at least a few Gyr (while the upturn in the SFR in both galaxies at about 5 Gyr ago, suggests their association may even extend further back in time).

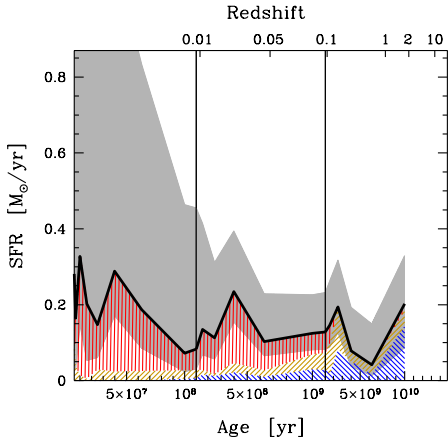


FIG. 19.— The integrated SFH solution for the Small Magellanic Cloud, adapted from Harris & Zaritsky (2004). The shading and colors are the same as in Figure 11.

5.3. The LMC’s Chemical Enrichment History

The chemical enrichment history (CEH) of a galaxy is the complement of its SFH, completing our understanding of the feedback cycles of star formation and stellar evolution. Over the past few decades, nearly a hundred LMC star clusters have had both an accurate age estimate from isochrone fitting to their CMDs, and a metallicity measurement from either spectroscopy or isochrone fitting. The resulting age-metallicity relation (AMR) for LMC star clusters provides perhaps the best available information on its CEH. Several constructions of the LMC’s cluster AMR exist, based on the best values in the literature at the time (Olszewski et al. 1996; Dirsch et al. 2000). We present an updated AMR in Figure 20, consisting of age and metallicity values of 85 LMC star clusters (the age and metallicity data were compiled from a literature search, and are tabulated in Appendix A). This is not necessarily a complete sample, nor has it been vetted to necessarily present the highest quality measurements. As one example of the latter, a recent study of four clusters (Mucciarelli et al. 2008) presents spectroscopic abundance measurements for three of the clusters in Appendix A. The differences in the abundance measurements as presented in the new study and our tabulated literature search are -0.23 , 0.00 , and -0.09 . While at least the largest of these differences would be problematic for certain issues, a quick inspection of Figure 20 reveals that both the scatter among clusters and the uncertainties in our measured chemical evolution render such difference irrelevant for the purpose at hand.

The essential features of the AMR have not changed: there is still a long “Age Gap”, a dearth of cluster formation interrupted only by the enigmatic ESO121-SC03. Prior to the Age Gap, the LMC formed a number of low-metallicity populous clusters, analogous to the Milky Way’s globular cluster population. Following the Age Gap, cluster formation resumed in the LMC, and proceeded roughly continuously to the present day. The

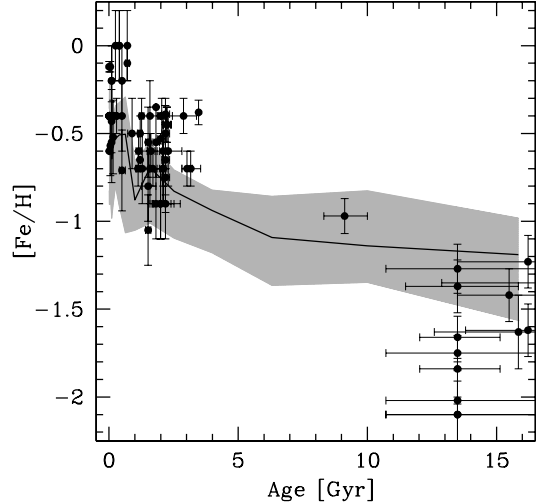


FIG. 20.— The Age-Metallicity Relation for the LMC. The points with errorbars are 85 LMC star clusters which have age and metallicity measurements in the literature. The mean metallicity as a function of age derived from our SFH analysis is shown as a heavy line, and its statistical variance is shown as a grey envelope. Our analysis contains only a single value for ages older than 4 Gyr, because we anchored the old SFH to published results based on deep HST imaging.

clusters formed following the Age Gap have a wide dispersion in metallicity, but they are significantly more enriched than the ancient cluster population, and there is some evidence for further enrichment with time for ages <4 Gyr.

Recently, Carrera et al. (2008) have examined the AMR for field stellar populations, based on Calcium triplet spectroscopy of individual red giants in four LMC fields. They find that the disk AMR is similar to that of the LMC star clusters: there was rapid initial enrichment to $[\text{Fe}/\text{H}] = -0.7$ by about 10 Gyr ago. Following this, the metallicity increased only slowly until 4 Gyr ago, when it began a more rapid increase to its present-day value of $[\text{Fe}/\text{H}] = -0.2$. While Carrera et al. do see some field stars with ages spanning the cluster Age Gap, their age uncertainties are necessarily large for individual stars, and their reconstructed SFH (for their inner disk fields) still indicates a quiescent epoch between 5 and 10 Gyr ago. These conclusions differ in detail from those derived from the AMR of the central region of the LMC (Cole et al. 2005), but the observed AMR are entirely consistent.

Detailed abundance measurements of individual LMC stars also show a chemical signature of this long quiescent epoch in the SFH (Tsujiimoto et al. 1995; Hill et al. 2000; Pompéia et al. 2008). The alpha-element abundances in these stars indicates that enrichment by Type Ia supernovae has been more important in the LMC than in the Milky Way, which implies that the cluster Age Gap was a general lull in the LMC’s star formation rate, and not simply the result of dynamical cluster destruction processes.

Into this context, we insert our reconstruction of the LMC’s CEH, based on the best-fit metallicities as a function of age in our StarFISH analysis. Photometry is an extremely blunt instrument with which to determine metallicities, even in a statistical analysis involving mil-

lions of stars. However, the best-fit SFH solutions show the bulk enrichment trend that is expected from the cyclical feedback processes of star formation and stellar evolution. This congruence with expectations gives us some confidence in at least the broad outlines of the chemical enrichment history encoded in our solutions.

We use the stellar mass formed during each age bin and at each metallicity to compute the stellar-mass weighted average metallicity as a function of age. This global mean age-metallicity relation is shown in Figure 20, overplotted with the LMC’s cluster AMR. We assign uncertainties to our metallicity estimates based on the difference between adjacent metallicity bins in our analysis and take symmetric error bars for bins on the edges of our range. Because we have tied the old SFH to the HST results, we have only a single best-fit metallicity for ages older than ~ 4 Gyr. Our reconstruction of the LMC’s CEH is qualitatively similar to the one we derived for the SMC (see Harris & Zaritsky 2004). In both galaxies, the mean metallicity remained at a constant low value, until about 4 Gyr ago when the metallicity began a steady ascent to the present-day value. In both galaxies, the age-metallicity relation from our analysis is consistent with that of the star clusters, and with the “bursting” enrichment model proposed by Pagel & Tautvaisienė (1999). Interestingly, the enrichment trend in the LMC appears to have two small interruptions at 1 Gyr and 100 Myr ago, but these episodes are only marginally significant.

6. SUMMARY

In this paper, we present the first global reconstruction of the SFH of the LMC, and indeed, the first global SFH solution for any galaxy as large as $0.1 L^*$. The SFH revealed by our solution is largely consistent with the LMC’s cluster formation history. There was an initial epoch of star formation during which a significant portion of the LMC’s stellar mass was formed. This era was followed by a long quiescent epoch, during which star formation was suppressed throughout the LMC. Then, about 5 Gyr ago, star formation resumed throughout the LMC, and has been ongoing since. The global resumption of star formation is strongly suggestive of a dramatic change in the LMC 5 Gyr ago, such as the merger of a gas-rich dwarf galaxy or a particularly dramatic tidal encounter, probably with the SMC given the similar resumption of star formation seen in that galaxy’s SFH.

The chemical enrichment history inferred from our analysis is also consistent with the cluster age-metallicity relation. The early history was characterized by rapid enrichment, reaching $[\text{Fe}/\text{H}]=-1.2$ by about 12 Gyr ago. The metallicity then remained stagnant throughout the long quiescent epoch. When star formation resumed 5 Gyr ago, the chemical abundances began a steady ascent to the present-day value of $[\text{Fe}/\text{H}]=-0.5$. The tight coupling between the field and cluster populations in the LMC, in both their star formation and chemical enrichment histories, argues for a strong connection between field and cluster “modes” of star formation in this galaxy.

Since star formation resumed 5 Gyr ago, the mean star formation rate has been approximately $0.2 M_{\odot} \text{ yr}^{-1}$, modulated by variations at the factor-of-two level. We note that our measured variations should be regarded as a lower limit, since strong deviations in the star formation rate can be undetected by our analysis if they are of

sufficiently short duration. We measure the total number of stars formed during an epoch, we cannot constrain whether the rate of star formation within that epoch was constant or highly variable.

There are several temporally coincident features in the global SFH solutions of the LMC and SMC. Both galaxies experienced a long quiescent epoch starting roughly 10 Gyr ago, and ending 5 Gyr ago in the LMC, and 3 Gyr ago in the SMC. Both galaxies experienced a significant peak in the star formation rate 2–3 Gyr ago. In the LMC, the stars that were formed during this event are now centrally concentrated in the LMC, although they don’t seem to conform to the contours of the LMC bar. In the SMC, the stars formed at this time are not centrally concentrated today; indeed, they seem to be distributed in a ring-like structure. Both galaxies also show enhanced star-formation activity around 400 Myr ago. These correlations suggest a common history for the Magellanic Clouds, stretching back over at least the past few Gyr.

We examine the spatial variation of the LMC’s SFH by comparing the integrated solutions for eight subregions in the SFH map. The SFH of the LMC bar is qualitatively similar to that of non-bar regions, indicating that the stars in the bar have likely always been part of the LMC. The SFHs of spiral-like “arms” extending off opposite ends of the bar are strikingly dissimilar. For example, the activity at 2.5 Gyr is very pronounced in the southeast arm, but is not distinguishable in the northwest arm. Also, the recent star formation rate peaked 600 Myr ago in the southeast arm, whereas the star formation rate in the northwest arm has climbed steadily over the past Gyr. The lack of symmetry in the histories of these “arm” structures suggests that these structures should not be regarded as a spiral-density wave phenomenon in the disk of the LMC. In a future paper, we will examine the spatial relationships of events in the LMC’s recent SFH in greater detail, with an eye toward revealing some of the physical processes driving star formation in the LMC disk.

The global SFH solution presented in this paper provides us with a unique opportunity to study galaxy evolution from a novel angle. Much of what we have learned about galaxy evolution comes from the study of large samples of galaxies at high redshift (cf. Lilly et al. 1996; Madau et al. 1996). In these studies, evolution is necessarily inferential, because no single galaxy can be followed through its history; we have only a series of “snapshots” showing the evolutionary state of populations of galaxies at a particular point in their history. The total SFH solution of the LMC represents a nearly ideal complement to the body of work on the evolution of galaxy populations at different redshifts: for a single galaxy, at least, we now possess the knowledge of its entire past history. Other dwarf galaxies have had complete SFH solutions, but the LMC is the first one that is massive enough to be well represented in large galaxy surveys out to at least $z = 1$. In a follow-up paper, we will place the LMC in its cosmological context by examining the evolution of its bulk properties, and by placing the evolutionary track of the LMC on well-known examinations of galaxy evolution from the galaxy-survey literature (such as the Madau-Lilly plot, the galaxy color-magnitude diagram, and galaxy scaling relations (Zaritsky et al. 2008)).

Acknowledgments: We are grateful to Sean Points and Chris Smith for providing us with the MCELS H α image of the LMC in advance of its publication. This work was partially supported by NASA through Hubble Fellowship grant HF-01160.01-A awarded by the Space Telescope Science Institute, which is operated by the Asso-

ciation of Universities for Research in Astronomy, Inc., under NASA contract NAS 5-26555. DZ acknowledges financial support from National Science Foundation CAREER grant AST-973311, AST-0307482, NASA LTSA award NNG05GE82G, and a fellowship from the David and Lucile Packard Foundation.

REFERENCES

- Alcock, C., Allsman, R. A., Alves, D. R., Axelrod, T. S., Becker, A. C., Bennett, D. P., Bersier, D. F., Cook, K. H., Freeman, K. C., Griest, K., Guern, J. A., Lehner, M., Marshall, S. L., Miniti, D., Peterson, B. A., Pratt, M. R., Quinn, P. J., Rodgers, A. W., Stubbs, C. W., Sutherland, W., Tomaney, A., Vandehai, T., & Welch, D. L. 1999, *AJ*, 117, 920
- Bekki, K., Couch, W. J., Beasley, M. A., Forbes, D. A., Chiba, M., & Da Costa, G. S. 2004, *ApJ*, 610, L93
- Bertelli, G., Mateo, M., Chiosi, C., & Bressan, A. 1992, *ApJ*, 388, 400
- Besla, G., Kallivayalil, N., Hernquist, L., Robertson, B., Cox, T. J., van der Marel, R. P., & Alcock, C. 2007, *ApJ*, 668, 949
- Bica, E., Geisler, D., Dottori, H., Clariá, J. J., Piatti, A. E., & Santos, Jr., J. F. C. 1998, *AJ*, 116, 723
- Brocato, E., Castellani, V., Ferraro, F. R., Piersimoni, A. M., & Testa, V. 1996, *MNRAS*, 282, 614
- Carrera, R., Gallart, C., Hardy, E., Aparicio, A., & Zinn, R. 2008, *AJ*, 135, 836
- Cole, A. A., Tolstoy, E., Gallagher, III, J. S., & Smecker-Hane, T. A. 2005, *AJ*, 129, 1465
- Da Costa, G. S. 1991, in *IAU Symp. 148: The Magellanic Clouds*, 183+
- Da Costa, G. S. & Hatzidimitriou, D. 1998, *AJ*, 115, 1934
- Dirsch, B., Richtler, T., Gieren, W. P., & Hilker, M. 2000, *A&A*, 360, 133
- Dolphin, A. E. 2000, *MNRAS*, 313, 281
- , 2002, *MNRAS*, 332, 91
- Ferraro, F. R., Mucciarelli, A., Carretta, E., & Origlia, L. 2006, *ApJ*, 645, L33
- Gallagher, J. S., Mould, J. R., de Feijter, E., Holtzman, J., Stappers, B., Watson, A., Trauger, J., Ballester, G. E., Burrows, C. J., Casertano, S., Clarke, J. T., Crisp, D., Griffiths, R. E., Hester, J. J., Hoessel, J., Krist, J., Matthews, L. D., Scowen, P. A., Stapelfeld, K. R., & Westphal, J. A. 1996, *ApJ*, 466, 732
- Gardiner, L. T., Sawa, T., & Fujimoto, M. 1994, *MNRAS*, 266, 567
- Geha, M. C., Holtzman, J. A., Mould, J. R., Gallagher, III, J. S., Watson, A. M., Cole, A. A., Grillmair, C. J., Stapelfeldt, K. R., Ballester, G. E., Burrows, C. J., Clarke, J. T., Crisp, D., Evans, R. W., Griffiths, R. E., Hester, J. J., Scowen, P. A., Trauger, J. T., & Westphal, J. A. 1998, *AJ*, 115, 1045
- Geisler, D., Piatti, A. E., Bica, E., & Clariá, J. J. 2003, *MNRAS*, 341, 771
- Gilmozzi, R., Kinney, E. K., Ewald, S. P., Panagia, N., & Romaniello, M. 1994, *ApJ*, 435, L43
- Girardi, L., Bertelli, G., Bressan, A., Chiosi, C., Groenewegen, M. A. T., Marigo, P., Salasnich, B., & Weiss, A. 2002, *A&A*, 391, 195
- Grocholski, A. J., Cole, A. A., Sarajedini, A., Geisler, D., & Smith, V. V. 2006, *AJ*, 132, 1630
- Hardy, E., Buonanno, R., Corsi, C. E., Janes, K. A., & Schommer, R. A. 1984, *ApJ*, 278, 592
- Harris, J. & Zaritsky, D. 2001, *ApJS*, 136, 25
- , 2004, *AJ*, 127, 1531
- , 2008, accepted for publication in *PASA*
- Hilker, M., Richtler, T., & Gieren, W. 1995, *A&A*, 294, 648
- Hill, R. S., Cheng, K.-P., Bohlin, R. C., O’Connell, R. W., Roberts, M. S., Smith, A. M., & Stecher, T. P. 1995, *ApJ*, 446, 622
- Hill, V., François, P., Spite, M., Primas, F., & Spite, F. 2000, *A&A*, 364, L19
- Hodge, P. W. 1960, *ApJ*, 131, 351
- , 1961, *ApJ*, 133, 413
- Holtzman, J. A., Gallagher, J. S., I., Cole, A. A., Mould, J. R., Grillmair, C. J., Ballester, G. E., Burrows, C. J., Clarke, J. T., Crisp, D., Evans, R. W., Griffiths, R. E., Hester, J. J., Hoessel, J. G., Scowen, P. A., Stapelfeldt, K. R., Trauger, J. T., & Watson, A. M. 1999, *AJ*, 118, 2262
- Hunter, D. A., Shaya, E. J., Holtzman, J. A., Light, R. M., O’Neil, Jr., E. J., & Lynds, R. 1995, *ApJ*, 448, 179
- Johnson, J. A., Bolte, M., Stetson, P. B., Hesser, J. E., & Somerville, R. S. 1999, *ApJ*, 527, 199
- Kallivayalil, N., van der Marel, R. P., Alcock, C., Axelrod, T., Cook, K. H., Drake, A. J., & Geha, M. 2006, *ApJ*, 638, 772
- Kerber, L. O., Santiago, B. X., & Brocato, E. 2007, *A&A*, 462, 139
- Kim, S., Staveley-Smith, L., Dopita, M. A., Freeman, K. C., Sault, R. J., Kesteven, M. J., & McConnell, D. 1998, *ApJ*, 503, 674
- Lilly, S. J., Le Fevre, O., Hammer, F., & Crampton, D. 1996, *ApJ*, 460, L1+
- Mackey, A. D. & Broby Nielsen, P. 2007, *MNRAS*, 379, 151
- Mackey, A. D. & Gilmore, G. F. 2004, *MNRAS*, 352, 153
- Mackey, A. D., Payne, M. J., & Gilmore, G. F. 2006, *MNRAS*, 369, 921
- Madau, P., Ferguson, H. C., Dickinson, M. E., Giavalisco, M., Steidel, C. C., & Fruchter, A. 1996, *MNRAS*, 283, 1388
- Meixner, M., Gordon, K. D., Indebetouw, R., Hora, J. L., Whitney, B., Blum, R., Reach, W., Bernard, J.-P., Meade, M., Babler, B., Engelbracht, C. W., For, B.-Q., Misselt, K., Vijn, U., Leitherer, C., Cohen, M., Churchwell, E. B., Boulanger, F., Frogel, J. A., Fukui, Y., Gallagher, J., Gorjian, V., Harris, J., Kelly, D., Kawamura, A., Kim, S., Latter, W. B., Madden, S., Markwick-Kemper, C., Mizuno, A., Mizuno, N., Mould, J., Nota, A., Oey, M. S., Olsen, K., Onishi, T., Paladini, R., Panagia, N., Perez-Gonzalez, P., Shibai, H., Sato, S., Smith, L., Staveley-Smith, L., Tielens, A. G. G. M., Ueta, T., Dyk, S. V., Volk, K., Werner, M., & Zaritsky, D. 2006, *AJ*, 132, 2268
- Mizuno, N., Yamaguchi, R., Mizuno, A., Rubio, M., Abe, R., Saito, H., Onishi, T., Yonekura, Y., Yamaguchi, N., Ogawa, H., & Fukui, Y. 2001, *PASJ*, 53, 971
- Mucciarelli, A., Carretta, E., Origlia, L., & Ferraro, F. R. 2008, *AJ*, 136, 375
- Nikolaev, S., Drake, A. J., Keller, S. C., Cook, K. H., Dalal, N., Griest, K., Welch, D. L., & Kanbur, S. M. 2004, *ApJ*, 601, 260
- Nikolaev, S. & Weinberg, M. D. 2000, *ApJ*, 542, 804
- Oey, M. S. & Massey, P. 1995, *ApJ*, 452, 210
- Olsen, K. A. G. 1999, *AJ*, 117, 2244
- Olsen, K. A. G., Hodge, P. W., Mateo, M., Olszewski, E. W., Schommer, R. A., Suntzeff, N. B., & Walker, A. R. 1998, *MNRAS*, 300, 665
- Olsen, K. A. G., Hodge, P. W., Wilcots, E. M., & Pastwick, L. 1997, *ApJ*, 475, 545
- Olszewski, E. W., Suntzeff, N. B., & Mateo, M. 1996, *ARA&A*, 34, 511
- Pagel, B. E. J. & Tautvaisienė, G. 1999, *Ap&SS*, 265, 461
- Payne-Gaposhkin, C. 1972, in *IAU Colloq. 17: Age des Etoiles*, ed. G. Cayrel de Strobel & A. M. Delplace, 3+
- Piatti, A. E., Bica, E., Geisler, D., & Clariá, J. J. 2003, *MNRAS*, 344, 965
- Piatti, A. E., Sarajedini, A., Geisler, D., Bica, E., & Clariá, J. J. 2002, *MNRAS*, 329, 556
- Points, S. 2008, mCELS H α image, private communication
- Pompéia, L., Hill, V., Spite, M., Cole, A., Primas, F., Romaniello, M., Pasquini, L., Cioni, M.-R., & Smecker Hane, T. 2008, *A&A*, 480, 379
- Sagar, R. & Pandey, A. K. 1989, *A&AS*, 79, 407
- Sagar, R. & Richtler, T. 1991, *A&A*, 250, 324
- Schinnerer, E., Böker, T., Emsellem, E., & Lisenfeld, U. 2006, *ApJ*, 649, 181
- Schwarzschild, M. 1958, *Structure and evolution of the stars*. (Princeton, Princeton University Press, 1958.)
- Smecker-Hane, T. A., Cole, A. A., Gallagher, J. S., & Stetson, P. B. 2002, *ApJ*, 566, 239
- Staveley-Smith, L., Kim, S., Calabretta, M. R., Haynes, R. F., & Kesteven, M. J. 2003, *MNRAS*, 339, 87
- Tsujimoto, T., Nomoto, K., Yoshii, Y., Hashimoto, M., Yanagida, S., & Thielemann, F.-K. 1995, *MNRAS*, 277, 945
- Vallenari, A., Aparicio, A., Fagotto, F., & Chiosi, C. 1994a, *A&A*, 284, 424

- Vallenari, A., Aparicio, A., Fagotto, F., Chiosi, C., Ortolani, S., & Meylan, G. 1994b, *A&A*, 284, 447
- van den Bergh, S. 1981, *A&AS*, 46, 79
- van der Marel, R. P., Alves, D. R., Hardy, E., & Suntzeff, N. B. 2002, *AJ*, 124, 2639
- van der Marel, R. P. & Cioni, M.-R. L. 2001, *AJ*, 122, 1807
- Will, J.-M., Bomans, D. J., Vallenari, A., Schmidt, J. H. K., & de Boer, K. S. 1996, *A&A*, 315, 125
- Woo, J.-H., Gallart, C., Demarque, P., Yi, S., & Zoccali, M. 2003, *AJ*, 125, 754
- Zaritsky, D. 1999, *AJ*, 118, 2824
- . 2004, *ApJ*, 614, L37
- Zaritsky, D. & Harris, J. 2004, *ApJ*, 604, 167
- Zaritsky, D., Harris, J., & Thompson, I. 1997, *AJ*, 114, 1002
- Zaritsky, D., Harris, J., Thompson, I. B., & Grebel, E. K. 2004, *AJ*, 128, 1606
- Zaritsky, D., Harris, J., Thompson, I. B., Grebel, E. K., & Massey, P. 2002, *AJ*, 123, 855
- Zaritsky, D., Schectman, S. A., & Bredthauer, G. 1996, *PASP*, 108, 104
- Zaritsky, D., Zabludoff, A. I., & Gonzalez, A. H. 2008, *ApJ*, 682, 68

APPENDIX

LMC CLUSTER AGES AND METALLICITIES FROM THE LITERATURE

Following Dirsch et al. (2000), we have collected a set of age and metallicity measurements of LMC stars clusters from the peer-review literature. The compiled data for 85 star clusters in the LMC are presented in Table A1; these are the cluster data we used in Figure 20. The cluster ages are derived from isochrone fitting in a CMD plane, and the metallicities are derived from spectroscopy or isochrone fitting.

TABLE A1
LMC CLUSTER AGES AND METALLICITIES

Cluster	[Fe/H]	$\sigma_{[Fe/H]}$	log(Age)	$\sigma_{\log(Age)}$	Reference	Notes
Reticulum	-1.66	0.12	10.13	0.05	Mackey & Gilmore (2004)	a
BRHTb	-0.40	0.0	8.0	0.0	Piatti et al. (2003)	bc
ESO121	-0.97	0.1	9.96	0.04	Mackey et al. (2006)	...
R136	-0.4	0.0	7.0	0.0	Hunter et al. (1995)	bc
OHSC33	-1.05	0.2	9.18	0.03	Bica et al. (1998)	...
OHSC37	-0.7	0.2	9.32	0.03	Bica et al. (1998)	...
Hodge11	-1.84	0.0	10.13	0.05	Grocholski et al. (2006)	ad
LH47/48	-0.4	0.0	6.3	0.0	Oey & Massey (1995)	bc
LH52/53	-0.4	0.0	7.0	0.0	Hill et al. (1995)	bc
LH72	-0.6	0.0	6.95	0.25	Olsen et al. (1997)	b
LH77	-0.4	0.0	7.20	0.14	Da Costa & Hatzidimitriou (1998)	b
LW224	0.0	0.2	8.85	0.0	Piatti et al. (2003)	c
SL8	-0.55	0.2	9.26	0.03	Bica et al. (1998)	...
SL126	-0.5	0.2	9.34	0.03	Bica et al. (1998)	...
SL218	-0.40	0.0	7.70	0.0	Piatti et al. (2003)	...
SL244	-0.7	0.2	9.11	0.09	Geisler et al. (2003)	e
SL262	-0.6	0.2	9.32	0.03	Bica et al. (1998)	...
SL359	-0.4	0.2	9.20	0.1	Geisler et al. (2003)	...
SL388	-0.39	0.05	9.34	0.03	Grocholski et al. (2006)	f
SL444	-0.4	0.2	8.7	0.0	Piatti et al. (2003)	c
SL446A	-0.9	0.2	9.34	0.1	Geisler et al. (2003)	...
SL451	-0.75	0.2	9.34	0.03	Bica et al. (1998)	...
SL503	-0.4	0.0	7.20	0.22	Da Costa & Hatzidimitriou (1998)	b
SL505	-0.5	0.2	8.95	0.09	Geisler et al. (2003)	...
SL506	-0.45	0.1	9.35	0.03	Kerber et al. (2007)	...
SL509	-0.65	0.0	9.08	0.0	Piatti et al. (2003)	bc
SL548	0.0	0.2	8.60	0.0	Piatti et al. (2003)	c
SL549	-0.9	0.2	9.30	0.1	Geisler et al. (2003)	...
SL555	-0.7	0.2	9.20	0.12	Geisler et al. (2003)	...
SL556	-0.7	0.2	9.32	0.0	Woo et al. (2003)	c
SL663	-0.7	0.1	9.50	0.05	Kerber et al. (2007)	e
SL674	-0.9	0.2	9.30	0.08	Geisler et al. (2003)	...
SL678	-0.8	0.2	9.18	0.08	Geisler et al. (2003)	...
SL769	-0.35	0.0	9.26	0.0	Piatti et al. (2003)	bc
SL817	-0.55	0.2	9.18	0.03	Bica et al. (1998)	...
SL842	-0.65	0.2	9.34	0.03	Bica et al. (1998)	...
SL862	-0.9	0.2	9.26	0.03	Bica et al. (1998)	...
SL896	-0.6	0.2	9.36	0.09	Piatti et al. (2002)	...
NGC1651	-0.53	0.03	9.30	0.03	Grocholski et al. (2006)	eg
NGC1711	-0.57	0.17	7.7	0.05	Dirsch et al. (2000)	...
NGC1718	-0.4	0.1	9.31	0.03	Kerber et al. (2007)	e
NGC1754	-1.42	0.15	10.19	0.06	Olsen et al. (1998)	...
NGC1777	-0.6	0.1	9.06	0.04	Kerber et al. (2007)	...
NGC1786	-2.1	0.3	10.13	0.1	Brocato et al. (1996)	h
NGC1806	-0.71	0.23	8.7	0.1	Dirsch et al. (2000)	...
NGC1831	-0.1	0.1	8.85	0.05	Kerber et al. (2007)	...
NGC1835	-1.62	0.15	10.21	0.07	Olsen et al. (1998)	...
NGC1836	0.0	0.2	8.60	0.0	Piatti et al. (2003)	c
NGC1838	-0.4	0.0	8.0	0.0	Piatti et al. (2003)	bc
NGC1839	-0.4	0.0	8.10	0.0	Piatti et al. (2003)	bc
NGC1841	-2.02	0.02	10.13	0.1	Grocholski et al. (2006)	ai
NGC1846	-0.40	0.0	9.3	0.03	Mackey & Broby Nielsen (2007)	b
NGC1850A	-0.12	0.03	7.7	0.1	Gilmozzi et al. (1994)	...
NGC1850B	-0.12	0.03	6.6	0.1	Gilmozzi et al. (1994)	...
NGC1856	-0.4	0.1	8.47	0.04	Kerber et al. (2007)	...
NGC1858	-0.4	0.0	6.9	0.0	Vallenari et al. (1994b)	bc
NGC1860	0.0	0.2	8.4	0.0	Piatti et al. (2003)	c
NGC1863	-0.40	0.0	7.7	0.0	Piatti et al. (2003)	bc
NGC1865	-0.2	0.2	8.7	0.0	Piatti et al. (2003)	c
NGC1866	-0.43	0.18	8.0	0.0	Hilker et al. (1995)	c
NGC1868	-0.7	0.1	9.05	0.03	Kerber et al. (2007)	...
NGC1898	-1.37	0.15	10.13	0.07	Olsen et al. (1998)	...
NGC1928	-1.27	0.14	10.13	0.1	Mackey & Gilmore (2004)	a
NGC1939	-2.10	0.19	10.13	0.1	Mackey & Gilmore (2004)	a
NGC1948	-0.4	0.0	6.85	0.15	Will et al. (1996)	b

TABLE 1
LMC CLUSTER AGES AND METALLICITIES (CONT.)

Cluster	[Fe/H]	$\sigma_{[Fe/H]}$	log(Age)	$\sigma_{\log(Age)}$	Reference	Notes
NGC1955	-0.4	0.0	7.19	0.15	Da Costa & Hatzidimitriou (1998)	b
NGC1978	-0.38	0.07	9.54	0.0	Ferraro et al. (2006)	ce
NGC2004	-0.4	0.0	7.19	0.15	Da Costa & Hatzidimitriou (1998)	be
NGC2005	-1.35	0.15	10.22	0.11	Olsen et al. (1998)	...
NGC2019	-1.23	0.15	10.21	0.08	Olsen et al. (1998)	...
NGC2027	-0.4	0.0	7.06	0.14	Da Costa & Hatzidimitriou (1998)	b
NGC2031	-0.52	0.21	8.2	0.1	Dirsch et al. (2000)	...
NGC2121	-0.4	0.1	9.46	0.07	Kerber et al. (2007)	e
NGC2134	-0.4	0.0	8.28	0.0	Vallenari et al. (1994a)	bc
NGC2136	-0.55	0.23	8.0	0.1	Dirsch et al. (2000)	...
NGC2155	-0.7	0.1	9.48	0.03	Kerber et al. (2007)	e
NGC2162	-0.4	0.1	9.10	0.03	Kerber et al. (2007)	...
NGC2164	-0.2	0.2	8.0	0.0	Sagar & Richtler (1991)	c
NGC2173	-0.6	0.1	9.21	0.04	Kerber et al. (2007)	e
NGC2209	-0.5	0.1	9.08	0.03	Kerber et al. (2007)	...
NGC2210	-1.75	0.1	10.13	0.1	Hill et al. (2000)	ehi
NGC2213	-0.7	0.1	9.23	0.04	Kerber et al. (2007)	e
NGC2214	-0.2	0.2	8.0	0.0	Sagar & Richtler (1991)	c
NGC2249	-0.45	0.1	9.35	0.03	Kerber et al. (2007)	...
NGC2257	-1.63	0.21	10.2	0.1	Dirsch et al. (2000)	...

^aage found to be “equal to M92”; age error is our estimate from isochrones

^bno [Fe/H] error given

^cno age error given

^dage reference: Johnson et al. (1999)

^ediscrepant [Fe/H] measurements exist in literature

^fage reference: Bica et al. (1998)

^gage reference: Kerber et al. (2007)

^hage found to be “equal to M68”; age error is our estimate from isochrones

ⁱage reference: Brocato et al. (1996)